

A new endstation for extreme-ultraviolet spectroscopy of free clusters and nanodroplets

Björn Bastian,¹ Jakob D. Asmussen,¹ Ltaief Ben Ltaief,¹ Achim Czasch,² Nykola C. Jones,¹ Søren V. Hoffmann,¹ Henrik B. Pedersen,¹ and Marcel Mudrich^{1, a)}

¹*Department of Physics and Astronomy, Aarhus University, Ny Munkegade 120, 8000 Aarhus C, Denmark*

²*Institut für Kernphysik, Goethe Universität, Max-von-Laue-Strasse 1, 60438 Frankfurt, Germany*

(Dated: 11 April 2022)

We present a new endstation for the AMOLine of the ASTRID2 synchrotron at Aarhus University, which combines a cluster and nanodroplet beam source with a velocity map imaging and time-of-flight spectrometer for coincidence imaging spectroscopy. Extreme-ultraviolet spectroscopy of free nanoparticles is a powerful tool for studying the photophysics and photochemistry of resonantly excited or ionized nanometer-sized condensed-phase systems. Here we demonstrate this capability by performing photoelectron-photoion coincidence (PEPICO) experiments with pure and doped superfluid helium nanodroplets. Different doping options and beam sources provide a versatile platform to generate various van der Waals clusters as well as He nanodroplets. We present a detailed characterization of the new setup and present examples of its use for measuring high-resolution yield spectra of charged particles, time-of-flight ion mass spectra, anion-cation coincidence spectra, multi-coincidence electron spectra and angular distributions. A particular focus of the research with this new endstation is on intermolecular charge and energy-transfer processes in heterogeneous nanosystems induced by valence-shell excitation and ionization.

I. INTRODUCTION

Synchrotron radiation has been used to study the structure and dynamics of atoms, molecules and clusters since the 1980s. Nevertheless, synchrotron spectroscopy of gas-phase targets still is an active research field today, due to the advantages of synchrotrons over lasers and other light sources: The enormous range of photon energies covered by synchrotrons, spanning from the infrared up to hard X-rays, is unchallenged by any other radiation source. State-of-the-art monochromator beamlines typically provide extremely narrow-band radiation ($E/\Delta E > 10^4$) continuously tunable across wide spectral ranges. This allows us to perform high-resolution spectroscopy in the extreme-

ultraviolet (EUV) or X-ray ranges, not accessible by other means.

Over the past decades, the focus of gas-phase synchrotron science has been shifting from mere atomic and molecular structure determination to unraveling the complex photophysics and photochemistry of free biomolecules and nanoparticles. Atomic and molecular clusters are ideal model systems with reduced complexity that enable detailed studies of relaxation dynamics in condensed phase systems initiated by valence-shell or inner-shell excitation or ionization. In particular, interatomic or intermolecular charge and energy transfer are fundamentally important relaxation processes of weakly bound molecules and nanosystems exposed to ultraviolet up to X-ray radiation. Nanoparticles are of great interest for modern applications due to their peculiar properties determined by finite-size effects; applications

^{a)}mudrich@phys.au.dk

range from heterogeneous photocatalysis¹, nanoplasmonics², aerosol science³, to radiation biology⁴.

Recent technical developments in synchrotron technology have mostly aimed to increase the achievable photon energy, brilliance and coherence of X-ray beams. In the particular field of gas-phase studies at synchrotrons, major progress has been made by devising more and more sophisticated diagnostic methods. Imaging detection of ions and electrons emitted by the irradiated molecules and nanoparticles provides both information about magnitudes and angles of electron and ion momenta. In particular, the velocity map imaging (VMI) technique⁵ is now widely used at EUV gas-phase beamlines because of its high particle momentum resolution and its 4π -collection efficiency. Additionally, the combination of VMI of electrons with time-of-flight (TOF) detection of ions, or vice versa, or even double-sided VMI detection, where the electrons and ions are detected in coincidence (photoelectron-photoion coincidence, PEPICO), are established techniques at many facilities nowadays^{6–14}.

Gas-phase synchrotron science is also being moved forward by devising and implementing more diverse sources of free molecular complexes, clusters and nanoparticles into EUV and X-ray beamlines. While biologically relevant molecules are mostly thermally evaporated¹⁵, supersonic jet expansions are also used, where the carrier gas is bubbled through water and passed over the sample vapor to form microhydrated clusters¹⁶. A slow-flow laser photolysis reactor in the vicinity of the ionization region is used to measure unimolecular and bimolecular reactions of free radicals¹⁷. Using the photon-ion merged-beams technique¹⁸, highly charged ions¹⁹, size-selected metal clusters²⁰, and endohedral fullerenes have been investigated²¹. By coupling an aerosol source to a synchrotron beamline, particles up to a size of $\sim 1 \mu\text{m}$ can be studied by EUV radiation^{22–24}.

Another attractive target system for EUV synchrotron studies is pure and doped superfluid helium (He) nanodroplets (HNDs)^{25,26}. Pioneering work by the groups of Toennies²⁷, Möller²⁸, and Neumark²⁹, have revealed complex relaxation dynamics of resonantly excited He nanodroplets, including visible and EUV fluorescence emission²⁸, autoionization causing the emission of ultraslow electrons³⁰, the ejection of mostly He_2^+ ions, and, to a lesser extent, larger fragment ions. Dopant molecules embedded inside the He droplets were found to be efficiently ionized indirectly by Penning-like excitation-transfer ionization via He^* ‘excitons’.^{27,31,32}

Neumark *et al.* introduced the VMI technique to study He nanodroplets in the photon energy range around the ionization energy of He, $E_i^{\text{He}} = 24.59 \text{ eV}$, using synchrotron radiation and later using laser-based EUV sources²⁹. In recent experiments at the synchrotron facility Elettra, Trieste, we have extended that work by implementing photoelectron-photoion coincidence (PEPICO) VMI detection. In this way, we can measure photoelectron spectra and angular distributions in coincidence with specific ion masses³³. We have evidenced efficient single and double ionization of alkali-metal atoms and molecules attached to the surface of He droplets, through resonantly excited He nanodroplets^{33–35}. Upon photoionization of the droplets, we found that embedded metal atoms are ionized by charge transfer mechanisms^{33,35,36}. We have recently complemented these synchrotron studies by time-resolved experiments using the tunable EUV free-electron laser Fermi, Trieste^{37–40}.

In this article we describe a new endstation that has recently been installed at the AMOLine of the ASTRID2 synchrotron at Aarhus University, Denmark⁴¹. With this apparatus, our previous experiments at Elettra^{33,35} will be further extended owing to a more sophisticated imaging detector, extended doping capabilities, improved options for cluster beam characterization, and vari-

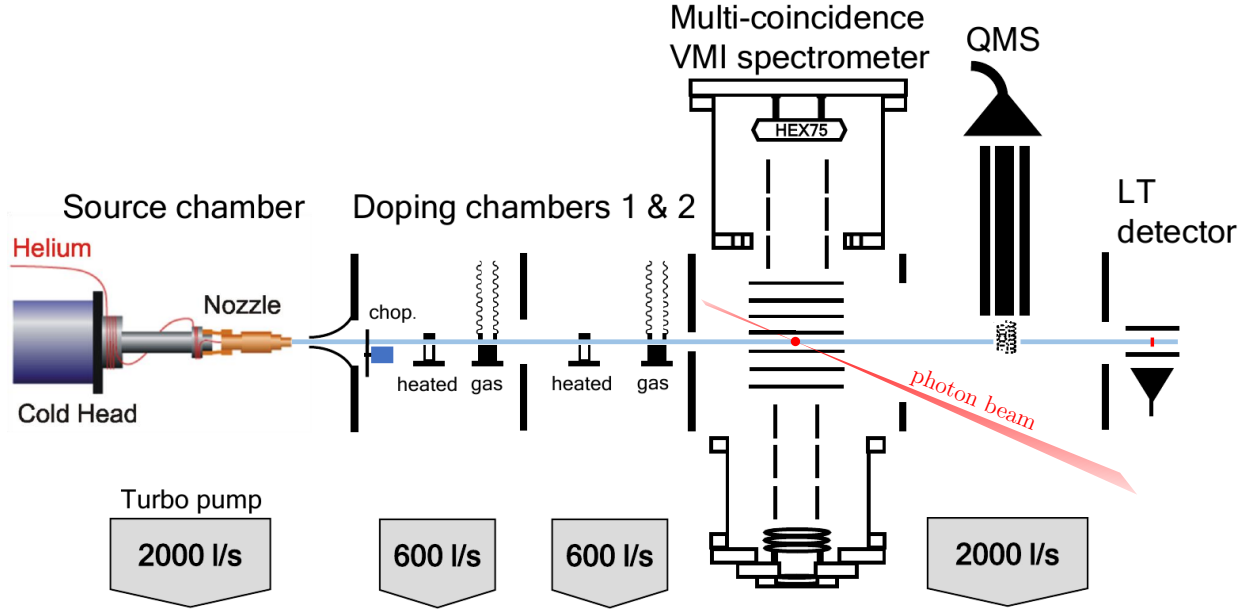


FIG. 1. Experimental setup. A skimmed He droplet beam is produced from a cryogenically cooled continuous nozzle expansion with 5 μm diameter. The chopper wheel (‘chop.’) allows to alternatively measure foreground and background. Gas doping and oven cells enable pickup of dopants by the droplets. The droplets then cross the photon beam in the center of the spectrometer. A quadrupole mass spectrometer (QMS) and Langmuir-Taylor detector (LT) behind the spectrometer are used for beam diagnostics.

ous cluster sources. We characterize the new PEPICO VMI spectrometer and present original data that illustrate the capability of the new setup to reveal the details of interatomic Coulombic decay (ICD) processes occurring in pure and doped He nanodroplets.⁴²

II. EXPERIMENTAL SETUP

The new endstation placed at the end of the AMOLine of the ASTRID2 synchrotron is schematically shown in Fig. 1. A skimmed atomic, molecular or cluster beam traverses two vacuum chambers for doping with gas and oven cells before crossing the photon beam from the synchrotron in the center of an ion–electron coincidence spectrometer. The molecular or cluster beam then passes a chamber housing a quadrupole mass spectrometer (QMS) and is dumped in an additional small chamber, which is directly at-

tached to the adjacent chamber without additional pumping. This beam dump also houses a simple Langmuir-Taylor (LT) detector for alkali and earth-alkali metals. Both chambers serve the purpose of monitoring the intensity and composition of the cluster beams. The pressure rise in the LT chamber in the presence of an He atomic or nanodroplet beam is on the order of 10^{-8} mbar.

For generating He nanodroplets we use a continuous cryogenic nozzle of diameter 5 μm placed at a distance of 12 mm in front of a skimmer with 0.4 mm diameter. Unless otherwise stated, all presented data were recorded with 30 bar He backing pressure and 14 K nozzle temperature. The average number of He atoms per droplet was estimated by titration measurements⁴³ that yielded $\langle N_{\text{He}} \rangle \approx 2000$. Typical operating pressures under these conditions are 1.4×10^{-3} mbar in the source, 4×10^{-6} mbar in the first and 6×10^{-7} mbar in the second doping chamber,

3×10^{-8} mbar in the VMI and QMS chambers and 5×10^{-8} mbar in the LT chamber.

A. The AMOLine at ASTRID2

A cross-section of the spectrometer chamber and the adjacent mirror chamber to couple in the photon beam from the AMOLine is presented in Fig. 2. Two different gratings for the monochromator (not shown) provide 5 to 150 eV photons from an undulator source on the ASTRID2 synchrotron. A slit and a selection of different foils can be used to adjust the photon intensity and suppress higher-order radiation. A focusing mirror after the monochromator is used to align the photon beam on the mirror (MC2) in Fig. 2 that refocuses the beam into the interaction region of the spectrometer (see Supporting Information S1). Several sets of scrapers placed upstream in the beamline are instrumental for reducing stray light reaching the mirror. The vertical position of the mirror is electronically controlled and can be replaced with either a photodiode or phosphor screen for photon beam diagnostics. The horizontal position (perpendicular to the beam direction) can be adjusted by movement of the chamber, while the pitch and yaw of the mirror are manually adjusted by a set of in-vacuum screws. The mirror chamber is separated from the spectrometer chamber by a pneumatic gate valve and a pinhole. The photon beam is dumped in a bent tube on the opposite side of the spectrometer which contains another phosphor screen and photodiode for beam diagnostics. Software integration of the data acquisition program and beamline control via TCP/IP allows several beamline parameters to be scanned for optimization, in particular the photon energy for automated photon-energy scans.

B. Beam source and doping options

A He atomic or nanodroplet beam is formed by a precooled continuous supersonic

expansion through a μm -size nozzle. The nozzle holder, body and He gas line are cooled by a closed-cycle cryostat that has a cooling power of 1 W at 4 K. A copper heat shield mounted on the first cooling stage is not shown in Fig. 1. The nozzle temperature is continuously measured and regulated by resistive heating. Nozzle openings are formed by planar Pt foils (orifice diameters 5, 10 or 20 μm) pressed into a copper holder. The open cylinder at the back of this holder is pressed onto a copper counterpart by a union nut and sealed with a C-shaped sealing ring. This facilitates the exchange of nozzles with different diameter. New nozzles are tested by measuring the He flow at 50 bar backing pressure, which typically amounts to 1 ml s^{-1} for a 5 μm nozzle. The supersonic expansion is skimmed to select the cold part of the beam before a shock wave is formed and for ensuring differential pumping. The skimmer holder is screwed into a threaded outer surface to adjust the nozzle-to-skimmer distance. The horizontal and vertical nozzle position can be varied by a translation stage without breaking vacuum.

To expand other gases, the same He nanodroplet source can be used where only the nozzle part has to be replaced by one with a larger diameter. Alternatively, it can be fully replaced by another beam source. A source for pure or molecule-doped water clusters based on the design of Förstel *et al.*⁴⁴ is currently in preparation.

In the oven chambers, four slots for heated ovens or gas doping cells enable sequential pickup of different dopants into He nanodroplets from solid, liquid or gaseous samples. This allows us to quickly apply different dopants or to form tailored multicomponent structures by adjusting the partial pressures and the order of doping the various substances into the droplet beam. The doping conditions are typically characterized by the QMS or by charge transfer ionization of dopants when irradiating the droplets with photons at energies $h\nu \geq E_i^{\text{He}}$.

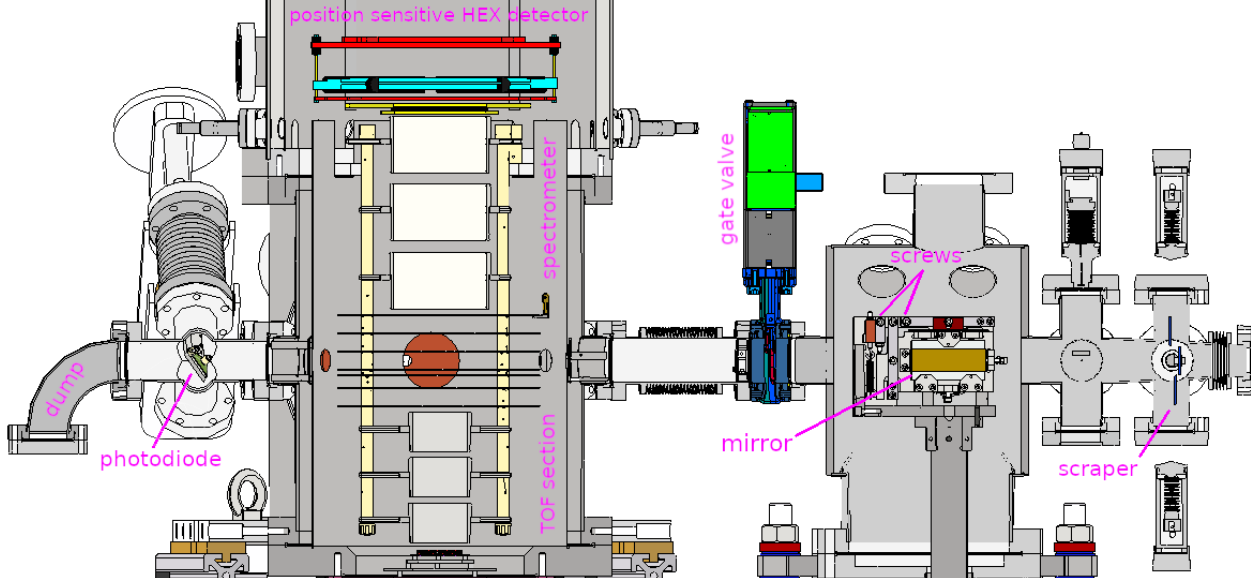


FIG. 2. Spectrometer with beam dump and photodiode (left) and grazing incidence mirror and scrapers (right) for the incoming photon beam.

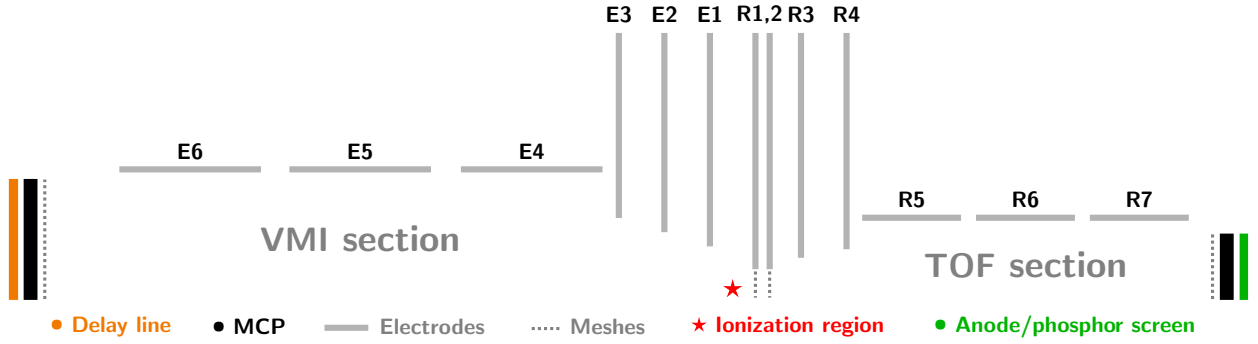


FIG. 3. Spectrometer geometry. Half of the central cross-section of the electrode stack is depicted true to scale, including the center of the ionization region on the central axis. The inner electrodes are realized by metal plates with concentric holes. The outer ion stacks in Einzel lens configuration are realized by metal cylinders. The black bars on the far left and right specify the detector positions. The lengths of the VMI and TOF sections from the ionization region to the detectors are 247 mm and 174 mm, respectively. Electrode positions and diameters are specified in Table I.

C. Spectrometer and VMI potentials

Two microchannel plate (MCP) detectors with a stack of μ -metal shielded electrodes and a position-sensitive detection system, see Fig. 2, are currently set up to measure kinetic energies on one side and ion flight times for mass spectrometry on the other side of the spectrometer. Coincidence detection of cations and electrons allows us to obtain the

ion time-of-flight (TOF) as the difference of electron and ion arrival times on the detectors. This detection mode is ideal for experiments with quasi-continuous photon beams as provided by synchrotrons.

The key strength of the electron and ion spectrometer is the combination of a RoentDek hexanode delay-line detector (HEX75)⁴⁵ with a set of electrodes to perform high-resolution VMI. The position-sensitive

TABLE I. Electrode positions and inner radii of the spectrometer in Fig. 3.

Electrode	E6	E5	E4	E3	E2	E1	R1	R2	R3	R4	R5	R6	R7
Position/mm	-190.625	-130.875	-70.625	-40.0	-24.0	-8.0	8.0	13.0	24.0	40.0	62.875	102.875	142.875
Radius/mm	42.0	42.0	42.0	25.0	20.0	15.0	7.0	7.0	11.0	14.0	25.0	25.0	25.0

HEX75 detector is well suited for single particle detection at high event rates⁴⁶ and in particular to reconstruct multi-hit events. In case of ion imaging, the < 1 ns time resolution facilitates the full three-dimensional reconstruction of the momentum vectors of several ions in Coulomb explosion experiments⁴⁷.

Fig. 3 shows a scaled drawing of the electrode configuration. The VMI section is similar to the spectrometer geometry at the GasPhase beamline at Elettra in Trieste, Italy¹⁰. A third extractor electrode is inserted and the flight tube is split into three tube sections to be used as an Einzel lens. The TOF and VMI sections of the spectrometer are separated by two meshes in the center that serve as repellers for VMI, labeled R1 and R2 in Fig. 3. The TOF section has a similar geometry with one electrode less, smaller electrode radius and shorter length. The time resolution does not noticeably depend on the specific electrode potentials, which are chosen to defocus the ions on the 40 mm diameter MCP to reduce wear (see Figure 9). The combination of the MCP with a phosphor screen and digital camera allows us to monitor the spatial distribution of ions on the detector. When removing the central meshes, VMI could be performed on both sides of the spectrometer. The delay-line detector is combined with a larger 80 mm diameter MCP which has the advantage of improved resolution when using higher VMI magnification and a larger maximum kinetic energy acceptance at a given magnification factor.

To achieve optimal VMI resolution it is crucial to optimize the potentials of the extractor electrodes to minimize the position spread due to the initial spatial distribution in the interaction region. The latter is de-

finied by the overlap of the focused photon beam and the droplet beam, of which the extent in the horizontal plane is restricted to 4 mm by a pair of adjustable scrapers. The three extractor electrodes and three electrodes in Einzel lens configuration are used to adjust the imaging properties to different ranges of electron kinetic energy. Trajectory simulations with the program SIMION⁴⁸ were used with a derivative based optimization routine⁴⁹ to refine different sets of electrode potentials for optimal VMI conditions in a simple and quick way (see also Supporting Information S2). In the original method, derivatives are evaluated at zero initial kinetic energy. Here, the method was extended to nonzero values.

To calibrate the spectrometer in spatial map imaging mode, potassium-doped He nanodroplets were ionized with a Coherent Mira Ti:sapphire laser at continuous 767 nm wavelength and about 0.56 W power. A lens with 175 mm focal length was mounted on a translation stage to focus the light into the center of the interaction region. By shifting the focus position in the interaction region horizontally and vertically, we calibrated the positions on the detector and the ion time-of-flight, respectively⁵⁰. Furthermore, a grating-stabilized diode laser is at our disposal to implement a simple scheme for photoionization of potassium atoms for precise calibration measurements⁵⁰.

III. RESULTS AND DISCUSSION

A. Velocity mapping and resolution

Precise velocity map imaging is the basis for accurate measurements of electron or ion

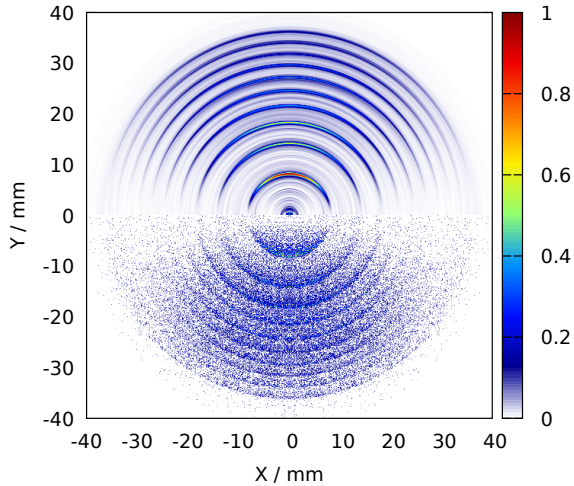


FIG. 4. Photoelectron images for the ionization of gas-phase He at photon energies of 26, 29, 32, 35, 38, 41, 44, 47, 50 and 53 eV. **Lower half:** Raw images. **Upper half:** Abel inverted distributions.

kinetic energy spectra and angular distributions. This section describes and characterizes different VMI potentials including scaled potentials to improve the resolution at low kinetic energies in the eV range and use of Einzel lens electrodes to achieve detection up to kinetic energies of 100 eV.

1. *Electron VMI without the Einzel lens*

Spectrometer potentials for high resolution VMI imaging were determined with the numerical optimization routine. We refer to the Supporting Information for additional details (S2) and the obtained potentials (Table S.3). For calibration and characterization, a set of He⁺ images from photoionization in the gas phase is acquired at equally spaced photon energies, see Fig. 4. The energy calibration with empirical and simulation results in Fig. 5a and Table II is detailed in the Supporting Information (S3).

The agreement of the near-linear calibration functions is very good with a maximum

TABLE II. Calibration coefficients for VMI without Einzel lens. The calibration function is $E_{\text{kin}} = p_0 R^2 + p_1 R^4 + p_2 R^6$. Uncertainties in parentheses are given in units of the last digit.

Origin	p_0	$p_1/10^{-7}$	$p_2/10^{-9}$
Experiment	0.0235(1)	21(3)	-1.5(1)
Simulation	0.023 58	1.13(2)	0.0013(8)
with offset	0.0260(4)	26(11)	-1.5(10)

deviation of 0.9% between simulation and measurement (black crosses in Fig. 5b). The higher-order coefficients p_1 and p_2 are not reproduced by the simulation. Their order of magnitude can be reproduced by a more detailed simulation taking into account an initial position distribution (see Supporting Information S4) that is offset from the center by 4 mm away from the detector and 9 mm along the photon beam (last row in Table II). Besides imperfect centering of the photon beam and the He beam, also small deviations from the ideal electrical field and residual magnetic fields may contribute to the nonlinearities.

2. *Energy resolution limits*

Quantifying the energy resolution by the ratio of the standard deviation ΔE to the magnitude of the electron kinetic energy E , the VMI settings without Einzel lens perform best with $\Delta E/E = 1.7\%$ at large detector radii. The resolution stays below 2.1% down to about 13 eV kinetic energy in Fig. 5b. Below 13 eV, the absolute radial spread stays constant near 230 μm so the energy resolution decreases and reaches 5% at 1.5 eV kinetic energy.

A position resolution of 160 μm ⁴⁶ FWHM and better can be achieved with the HEX75 detector for atoms and ions, corresponding to a standard deviation of 68 μm . Electrons produce signal amplitudes with lower magnitude and higher variance and we expect a resolution limit of 100 μm represented by the gray line in Fig. 5b. The simulated energy

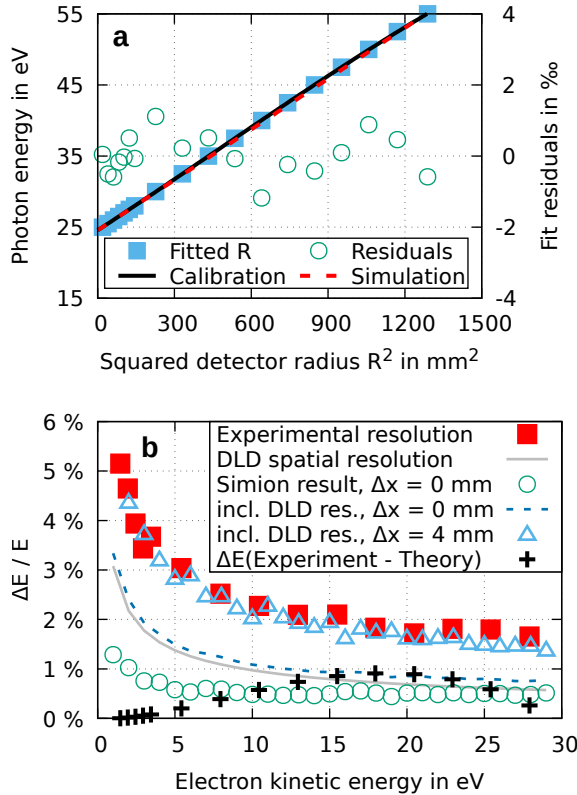


FIG. 5. Results of a calibration measurement in comparison with simulation results. (a) Photon energy as a function of the squared detector radius with a polynomial fit. (b) Experimental data above 70 eV kinetic energy as the high energy resolution, simulated deviations due to off-center start positions and relative deviation between the simulated and the empiric calibration function.

broadening (see details in Supporting Information S4) due to the initial spatial distribution in the interaction region (green circles) only slightly raises this resolution limit (blue dashed line) that stays more than a factor 2 below the experimental resolution. One possible explanation is the so far not controlled vertical position of the photon beam: The assumption of a 4 mm offset from center irrespectively of the direction mostly reproduces the experimental result (blue triangles). The horizontal position has a minor effect on the simulated resolution. A later improvement of the detector resolution with higher MCP gain

did not result into a better experimental resolution which supports the hypothesis that adjustment of the interplay between vertical position and electrode potentials may further improve the achieved energy resolution.

Alternative potentials with improved resolution for low and high electron kinetic energy ranges are presented in the following.

3. Alternative VMI potentials

The maximum kinetic energy acceptance with -3.5 kV extraction potential without using the Einzel lens is about 32 eV. In highly excited or core ionized systems, it is often desirable to capture faster electrons to probe the process of interest or to include photoelectrons from direct ionization as a reference, e.g. to determine branching ratios.

We have achieved compression of electron VMI images with identical positive potentials on the outer electrodes E4, E6 of the Einzel lens and refer to the Supporting Information (S2) for additional explanations. The calibration curves in Fig. 6b visualize the resulting energy acceptance. There is no empirical data above 70 eV kinetic energy as the high energy grating for the monochromator was not available when the data were taken.

Simply adding 6 kV potentials to the optimized potentials without the lens gives the highest energy acceptance up to 100 eV but significantly decreases the energy resolution, see Fig. 6c ("Unopt. lens", blue triangles). Numerical re-optimization for VMI conditions almost restores the original energy resolution (yellow diamonds) at the cost of somewhat lower 90 eV maximum energy.

Optimized potentials with a 3.5 kV Einzel lens are a good compromise with 50 eV energy acceptance and excellent resolution reaching down to 1.2% in the high-energy range.

The energy resolution decreases quickly at low energies in the 1 eV range and this would still be true if the spatial resolution limit of the detector (gray line) could be reached.

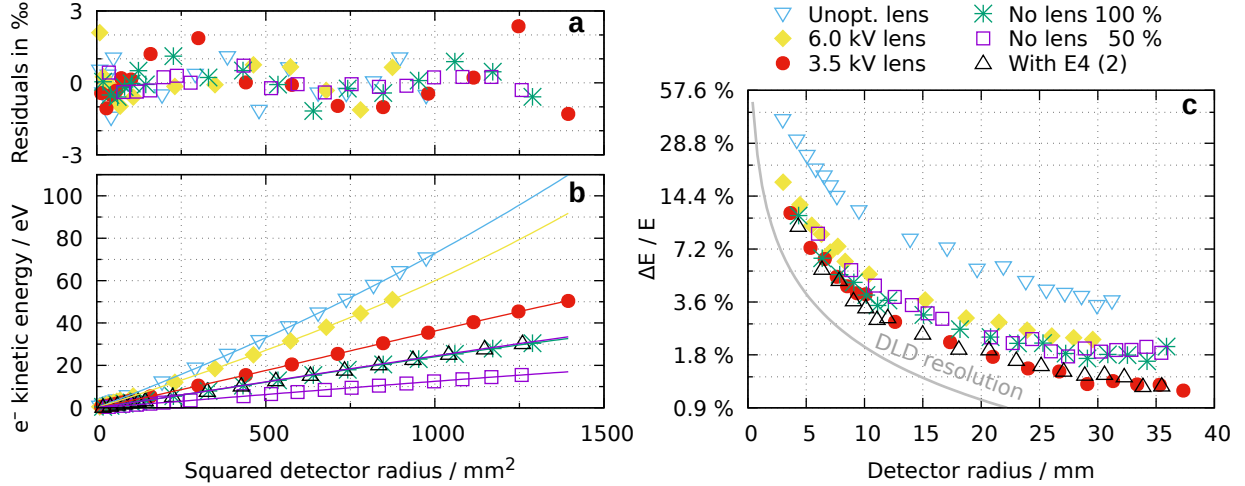


FIG. 6. Fit residuals (a), calibration fits (b) and energy resolution (c) for different VMI settings. The corresponding electrode potentials are specified in Table S.3. The gray line indicates the expected resolution limit of the HEX75 detector for electrons.

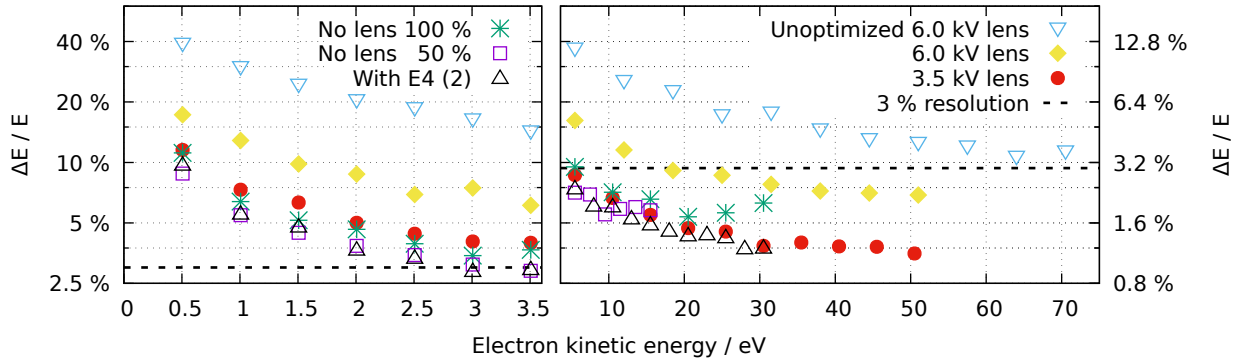


FIG. 7. Energy resolution as a function of electron kinetic energy for different VMI settings. The corresponding electrode potentials are specified in Table S.3. The 6 kV Einzel lens settings are applicable up to 90 eV and above (see Fig. 6b) which has not been recorded. The x range is split in two parts with different y ranges. Dashed lines at 3% resolution are shown to guide the eye.

Therefore, a larger velocity magnification factor is required to significantly improve the resolution for slow electrons. This can to some extent be achieved by scaling the extraction potentials and is demonstrated for the settings without an Einzel lens scaled to 100% (stars) and 50% (squares) of the full potentials. While the resolution as a function of radius cannot be substantially altered (Fig. 6c), the resolution at a specific energy is improved. This becomes evident in Fig. 7, which summarizes all settings with the res-

olution as a function of kinetic energy. The 50% results demonstrate the limits of this approach: scaling the potentials by a factor of 2 improved the resolution by merely 15% and settings below 30% potentials were empirically found to be inadequate for imaging.

The 100% potentials can be further improved by using lens E4 while the other two electrodes of the Einzel lens are kept at ground potential. Settings optimized for 30 eV kinetic energy (see Supporting Information Table S.3) reach the resolution of the

50 % potentials without compromising the kinetic energy acceptance in Fig. 7. The disadvantage is a significantly reduced time-of-flight resolution due to a shallower extraction potential ("low res." in Fig. 10).

Another elegant approach for low kinetic energies is to use a short Einzel lens in the flight tube to magnify the spatial distribution by inversion⁵¹. Ramping up the lens first focuses electrons of different kinetic energy until reaching inversion and then starts magnifying the inverted electron image. To be efficient, this approach requires a shorter Einzel lens with smaller diameter than in our spectrometer geometry. The original geometry would thus limit the spectrometer to relatively low kinetic energies. Furthermore, such a geometry reduces the VMI quality with a significant dependence on the initial particle position in a way that cannot be compensated for by the numerical optimization routine. A more detailed analysis will be required to evaluate the trade-off between the different sources of uncertainty.

B. Spatial mapping and beam overlap

1. SMI potentials and calibration

In analogy to VMI but with inverse logic, the spectrometer can be used for spatial map imaging (SMI) in the interaction region with high precision, irrespectively of the initial velocities of the imaged particles.⁴⁹ We have employed two-dimensional SMI for calibration and to characterize the overlap of the photon and He beam in the scattering plane. The numerical optimization routine was employed to determine potentials for three different settings that are presented in the Supporting Information (S5): (1) two-dimensional SMI of radial positions, (2) magnified two-dimensional SMI and (3) one-dimensional TOF-SMI of axial positions.

Calibration measurements for SMI settings were performed by ionizing potassium

doped HNDs at 767 nm wavelength. The magnification factor for ion or electron SMI was found to be -3.2 , in excellent agreement with the simulation value -3.154 (1.5 % deviation). With the magnifying settings, a factor of -13 was found (3 % deviation) and the TOF-SMI has a scaling factor of 64 ns mm^{-1} (10 % deviation).

2. SMI resolution

Cation SMI with K^+ ions gives an upper bound standard deviation of $50 \mu\text{m}$ for the waist of the focused beam (see Supporting Information, Table S.6). This corresponds to a radius of $160 \mu\text{m}$ on the detector, larger than the expected spatial resolution of the HEX75 detector of about $70 \mu\text{m}$ or lower. The same width is observed for the magnifying settings, which however corresponds to $670 \mu\text{m}$ on the detector. We assume that this is caused by stronger velocity broadening in line with the simulations that predict a significant derivative of the impact position with respect to the initial ion velocity, see Supporting Information (S5). The TOF-SMI settings give a similar value of $50 \mu\text{m}$ for the vertical direction which corresponds to a standard deviation of 3 ns in the ion flight times which is larger than the optimum time resolution of the HEX75 detector of about 0.5 ns .

With electron SMI at full and 50 % potentials (scaling $s = 1$ and 0.5), the standard deviations are $w = 80 \mu\text{m}$ and $110 \mu\text{m}$. The simplified assumption $w = w_0 + c/\sqrt{s}$ with beam waist w_0 and velocity dependent broadening thus gives the estimate $w_0 \approx 7.6 \mu\text{m}$. The order of magnitude is confirmed by the $8.5 \mu\text{m}$ focused spot radius of a Gaussian beam with 5 mm radius at the focusing lens. The experimental conditions are therefore suited to assess the resolution of about $50 \mu\text{m}$ (RMS) for ions that is achieved with the SMI mode.

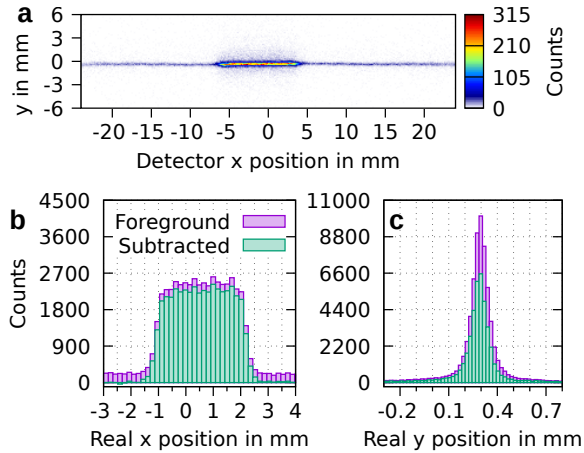


FIG. 8. Cation spatial map image (a), and its projections on the He beam (b) and photon beam (c) axis. A HND beam at 30 bar backing pressure and 12 K nozzle temperature is ionized by 25 eV photons. Ionization of the background gas makes the photon beam visible and is subtracted from the projections to show the droplet related contribution. The conversion to real position is detailed in Supporting Information S5.

3. Width of the He droplet beam

For a cold HND beam ionized at the synchrotron at 25 eV photon energy, the raw SMI image on the detector and the centered projections in units of real length are shown in Fig. 8. The presented data are not mass selected, such that the photon beam is clearly visible from ionized background gas. The measurements were performed with a running chopper wheel. The rising and falling edges of a TTL monitor signal were acquired with the TDC to filter foreground and background events in the data analysis. Fig. 8b demonstrates the clear isolation of the droplet related signal by subtraction. The full width of the droplet beam profile at the baseline is 4.3 mm, close to the 4 mm width of the scrapers that limit the horizontal extension of the droplet beam. The FWHM of a Gaussian fit to the photon beam profile is 0.12 mm in good agreement with an estimate of 0.11 mm derived from ray-tracing results

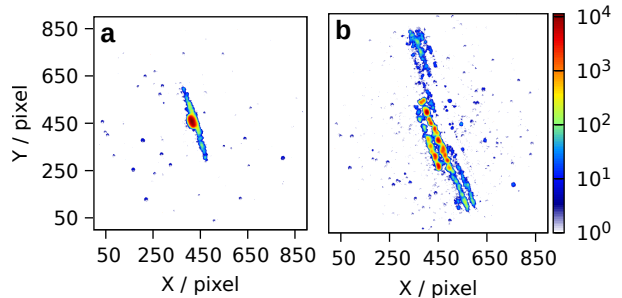


FIG. 9. Defocusing ions on the TOF detector. Electrode potentials are E1: -1433.5 V, R1/R2: -1750 V, R5/R7: -3550 V and R6: -4250 V. The MCP front and R6 potentials are the same. (a) Focused ions with $R3 = R2$ and $R4 = R5$. (b) Defocused ions with $R3 = R4 = -3000$ V.

in the Supporting Information (S1).

C. Time-of-flight mass spectrometry

Currently two meshes separate the VMI section from the TOF section which impedes to use the latter for velocity mapping. In principle, the TOF section can be used to collect electrons that define a zero point in arrival time to perform mass selective cation imaging in continuous beam experiments. In case of electron imaging, the TOF section provides complimentary information on the mass of coincident cations which is a powerful tool to probe if different ion formation channels involve different electronic states.

It has been found that the specific potentials of the electrodes in the TOF section (see Fig. 3) have only a small effect on the time resolution. Therefore, the potentials can be chosen to defocus the ions to increase the detector lifetime. This is demonstrated by an integrated intensity image of the phosphor screen in Fig. 9.

Two example mass spectra are presented in Fig. 10. The first shows a progression of clusters from a pure He beam. The droplets were ionized at 67.5 eV above the first excited level of He^+ . Some He_n^+ peaks are mixed with water, nitrogen, oxygen and carbon dioxide

and their fragments from the background gas in the VMI chamber that also contains He^+ from effusive He. Double electron coincidences from direct ionization and subsequent ICD at this photon energy are presented below.

The second mass spectrum shows the mass resolution achieved with the 100% VMI settings without using the Einzel lens electrodes. For these data, HNDs were doped with the nucleobase thymine (oven heated to 100 °C, $\sim 9.6 \times 10^{-6}$ mbar vapor pressure⁵²) and deuterated water (3.3×10^{-6} mbar partial pressure leaked directly into the vacuum chamber). The nucleobase was ionized and fragmented by either Penning ionization from He excited at a photon energy $h\nu = 21.6$ eV or by charge transfer to He ionized at $h\nu = 27$ eV. Single mass peaks are resolved up to around 40 u, still clearly visible around 80 u and start to convolute around 120 u. This allows us to identify several thymine fragments with different hydrogen content and mixed clusters with up to 4 attached heavy water molecules. Also pure water clusters up to $n = 3$ are seen. The protonated water complex $(\text{D}_2\text{O})_3\text{D}^+$ is indicative for the presence of larger clusters. Charge transfer leads to stronger fragmentation of thymine- D_2O complexes and thymine clusters, whereas in the case of Penning ionization, larger clusters and thymine dimers are present in the spectrum.

D. Energy scan of a Fano resonance

Double excitation into the He 2s2p state at $h\nu = 60.15$ eV gives rise to an atomic Fano resonance that is broadened and shifted to around 60.4 eV in He nanodroplets⁵³. The autoionization of a doubly excited atom can compete with the ionization of a neighbor atom. The second process is called Interatomic Coulombic Decay (ICD) and results into a lower electron kinetic energy (eKE). This has been theoretically shown for HeNe dimers, where ICD is increasingly competitive with excitation into higher Rydberg or-

bitals⁵⁴. Unfortunately, investigating ICD between neighboring He atoms in HNDs is complicated by inelastic scattering of the photoelectron⁵⁵ giving rise to the same eKE if the same singly excited state is involved, e.g. 1s2p. The inelastic scattering rate is expected to follow the Fano line shape of the photoline. In that case the ratio between low and high eKE would remain constant. If, however, ICD contributed to the electron yield, we would expect a pronounced increase of this ratio at the double excitation resonance.

We therefore performed detailed photon energy scans around the 60.4 eV and higher resonances that will be presented in a separate publication. The VMI potentials with a 3.5 kV Einzel lens were ideally suited for these measurements, providing excellent resolution and a wide electron kinetic energy range including photoelectrons (see Fig. 7). Fig. 11 shows an example of two electron images recorded in coincidence with He^+ and He_2^+ and the total eKE distributions at different photon energies. The photoline originates from direct ionization and autoionization while the 1s2p peak is due to ICD or inelastic scattering. We can thus compare relative rates as a function of selected electron/ion coincidences, electron kinetic energy and photon energy.

The He^+ coincidence image in Fig. 11a is background subtracted to remove the contribution of background He to the photoline (the He_2^+ image is background free). In general, the background-subtraction factor is corrected as described in the Supporting Information (S6). To obtain energy distributions, foreground and background images are inverted separately using MEVELER to avoid pixel noise and to fulfill the requirement of Poissonian statistics⁵⁶.

The electron images additionally contain angular information. Distributions of the angle θ between the photoelectron velocity vector and the polarization axis at 60.39 eV photon energy are presented in Fig. 12 with

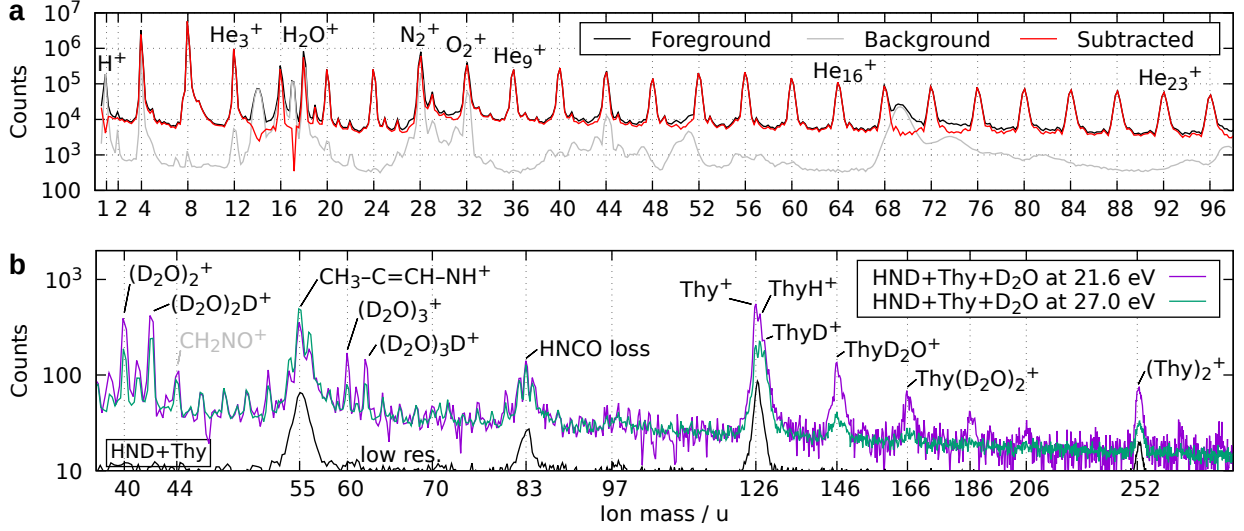


FIG. 10. Mass spectra of (a) pure HNDs ($h\nu = 67.5$ eV) and (b) HNDs doped with thymine and D_2O where dopants are Penning ionized (21.6 eV) and charge-transfer ionized (27 eV). Acquisition times were about 20 h (21.6 eV) and 6.5 h (27 eV) and the data of the latter are scaled by a factor of 0.3. The mass spectra in (b) are background subtracted. The solid black line shows a mass spectrum without D_2O and with reduced TOF resolution at 21.6 eV photon energy.

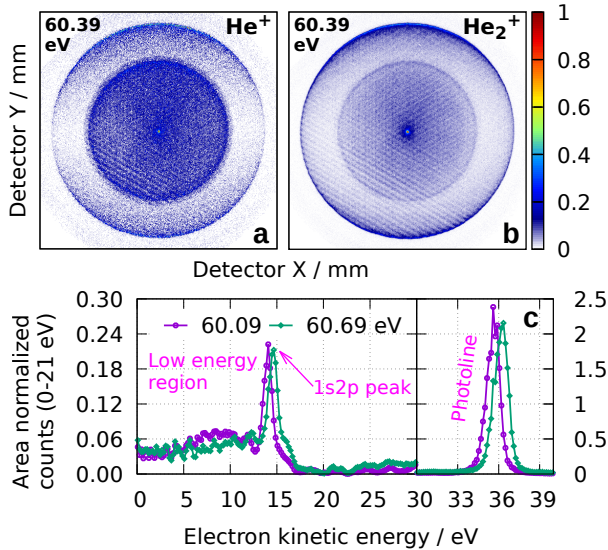


FIG. 11. Electron images in coincidence with (a) He^+ and (b) He_2^+ ions and (c) total eKE distributions at different photon energies around the 2s2p HND resonance (30 bar backing pressure, 14 K nozzle). The He^+ coincidence image and total eKE spectra are background subtracted.

fit results for the anisotropy parameter β . The background-subtracted droplet contribution from the photoline in coincidence with He^+ slightly deviates from the nearly perfect $\cos^2 \theta$ dependence as measured for background He atoms. This indicates a deflection of the emitted electrons presumably by elastic scattering of the electrons at He atoms. The He_2^+ photoline has a strong isotropic contribution and the low-kinetic-energy electrons (< 22 eV in Fig. 11) are predominantly isotropic due to massive elastic and inelastic electron- He scattering. A detailed analysis of the electron angular distributions of He nanodroplets will be presented elsewhere.

The narrow lineshape of the atomic 2s2p Fano resonance allows us to determine the energy resolution of the photon beam in the given energy range. To this end, we convolute the Fano line shape⁵⁷ with a Gaussian function as described by Domke *et al.*⁵⁸ The standard deviation of the Gaussian is determined by a least-squares fit, see Fig. 13. The energy resolution depends on the width of the monochromator exit slit. Measurements

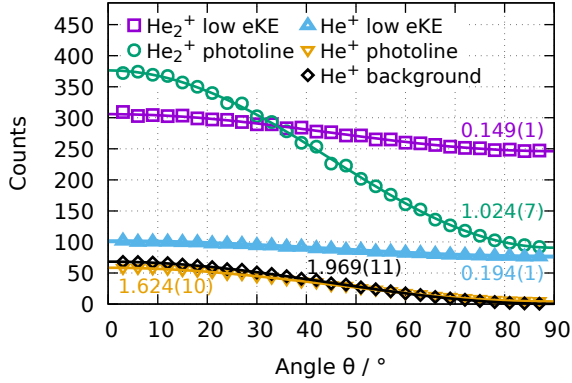


FIG. 12. Angle distributions at 60.39 eV photon energy. Solid lines are $1 + \frac{\beta}{2} (3 \cos^2 \theta - 1)$ fits. Resulting β -values are shown in the same color. The curve for the He^+ photoline is background subtracted.

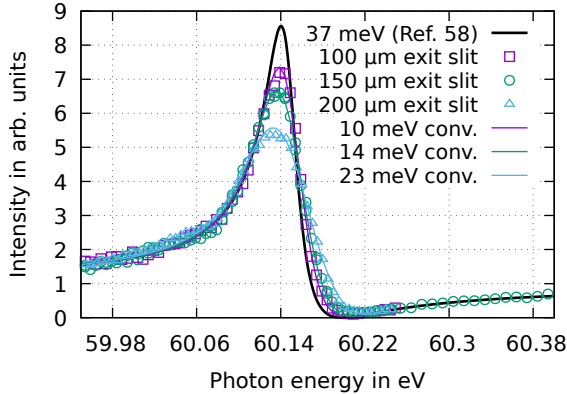
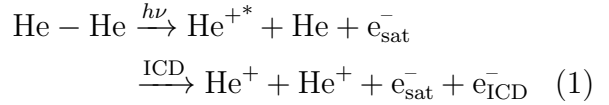


FIG. 13. Least-squares fits to an atomic Fano resonance for different monochromator exit slit widths. Gaussian functions with the specified widths are convoluted with the Fano profile (black curve) with parameters by Domke *et al.*⁵⁸

are usually taken with 150 μm exit-slit width corresponding to an absolute photon energy resolution of 14 meV or a resolving power of 4300. By further reducing the slit width to 100 μm the resolution can be further improved to 10 meV, at the cost of reduced photon flux, though. The measurement of the atomic Fano resonance position is also used for absolute energy calibration of the beamline.

E. Coincidences and multi-hits

Owing to the multi-hit capability of the HEX75 detector, it is possible to record two electrons from the same ionization event. By identifying coincidences both between electrons and between ions and electrons, we can select specific ionization processes in the analysis. To demonstrate the capability of this detection scheme, we revisit a previous experiment done at the GasPhase beamline at Elettra⁴². There, we studied Interatomic Coulombic Decay (ICD) in pure He nanodroplets upon formation of an excited He ion through the shake-up process.



The total number of charged particles from the process is then 4 (two electrons and two cations). In our previous study of this process, detection of two ions with different masses in coincidence with a single electron was possible, but detection of multi-hits of electrons was impossible; only a single electron was measured for each ionization event. With our new endstation, detection of all products of the ICD process is now possible. Furthermore, with our optimized VMI settings using the Einzel lens (see section III A 3), we can image the electrons from direct photoionization ($E_{\text{kin}} = h\nu - E_i^{\text{He}}$) as well as the satellite photoelectron (e_{sat}^-) from shake-up ionization and the ICD electron (e_{ICD}^-).

Figure 14 displays coincidences between two ions recorded at 67.5 eV. Detection of two ions with identical mass-to-charge ratio is impossible for the current use of the ion detector because they have nearly equal flight times and thus one ion arrives within the deadtime of the detector caused by the other ion. The most abundant ion-ion coincidence is the ion pair $\text{He}^+/\text{He}_2^+$. Simultaneously detected two He_k^+ ions stem from either ICD or impact ionization following direct photoion-

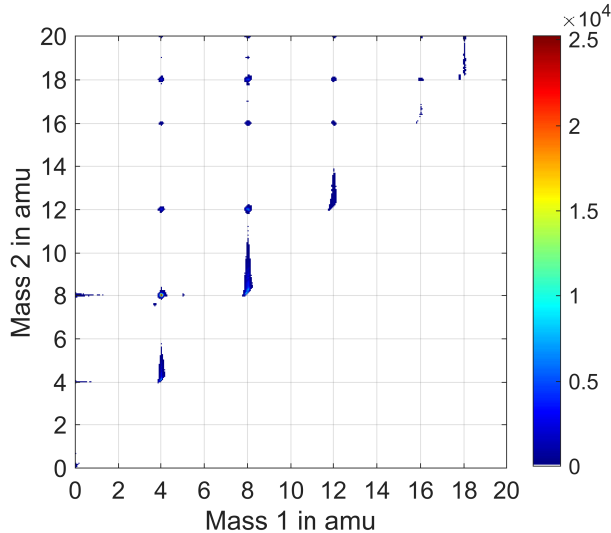


FIG. 14. Background-subtracted electron/ion/ion coincidence time-of-flight mass spectrum recorded at 67.5 eV photon energy, 30 bar backing pressure and 14 K nozzle temperature.

ization. The different ionization processes can be identified by inspecting the electron kinetic energy spectra. Figure 15 displays electron spectra for various cuts on the coincidence data recorded at 67.5 eV. From the coincidences of a single electron with either the He^+ or He_2^+ ion, we can identify four peaks in the spectra. The peak at ~ 43 eV is due to photoelectrons emitted by direct photoionization, whereas the peak at ~ 22 eV is due to inelastic scattering of the photoelectron with another He atom in the droplet⁵⁵. In the case of direct photoionization in coincidence with He^+ , the photoline stems from the component of free atoms accompanying the droplet beam.⁵⁵ The sharp line at 2.2 eV corresponds to satellite electrons, e_{sat}^- , and the broad feature centered around 8 eV are ICD electrons, e_{ICD}^- .

Direct photoionization and inelastic electron-He scattering leading to He excitation are processes creating only a single electron/cation pair. Therefore, the two peaks from these processes are suppressed in the electron spectra for coincidences of

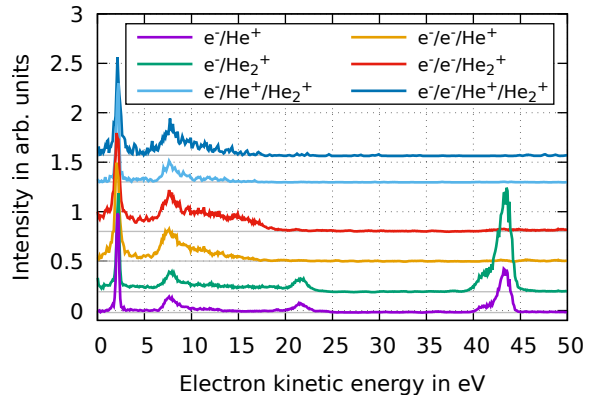


FIG. 15. Electron kinetic energy distribution for different coincidences recorded at 67.5 eV photon energy (nozzle at 14 K and 30 bar). In the case of coincidences involving two electrons, the spectrum contains the sum of the two electrons.

more than one electron and/or ion. The e_{sat}^- and e_{ICD}^- electrons are present in the spectra for all shown coincidence schemes, which shows that by selecting a certain coincidence scheme, we can filter for a specific ionization channel—in this case ICD. The two electrons from the ICD process arrive at the detector nearly at the same time such that we cannot separate them into two images. Instead, the spectra for coincidences of two electrons with one or two ions show the sum of the two electrons from each event. Setting the condition that the two electrons arrive at the detector simultaneously ($\Delta t < 10$ ns) helps to significantly suppress false coincidences. Differences in the shape of the ICD feature are seen depending on whether the coincidence cut includes the He^+ ion or only the He_2^+ ion. In triple $e^-/e^-/\text{He}_2^+$ coincidences, the ICD feature extends to higher kinetic energy compared to the ICD feature for $e^-/e^-/\text{He}^+$ coincidences. ICD between two He atoms at a larger interatomic distance leads to an increased kinetic energy of the electron in connection with a decreased kinetic energy release of the ions from Coulomb explosion⁵⁹. Thus, the high kinetic energy part in the ICD electron peak

for $e^-/e^-/\text{He}_2^+$ coincidences is due to ICD between two He atoms at large interatomic distance, which after ionization are more likely to pick up other He atoms before leaving the droplet due to their reduced kinetic energy. Consequently, the detection of this high-energy part of the ICD feature is suppressed for $e^-/e^-/\text{He}^+$ coincidences.

As already mentioned, electron impact ionization following direct photoionization can also lead to two electron/cation-pairs. The characteristic feature for impact ionization would be a broad feature reaching from zero kinetic energy to the excess energy following impact ionization ($h\nu - 2E_i^{\text{He}} = 18.3\text{ eV}$) due to uniformly distributed energy sharing between the two electrons⁵⁵. This is clearly seen in the $e^-/e^-/\text{He}_2^+$ coincidences in agreement with the formation of He_2^+ after the creation of a slow ion by electron impact. In most other channels, a clear minimum of zero intensity is present between the e_{sat}^- and e_{ICD}^- peaks, so we conclude a minor importance of impact ionization.

From the detection of either a single electron or the two electrons from the ICD process, we can estimate the detection efficiency of electrons on the HEX75 detector using the following formulas

$$f_1 = df_{\text{tot}} - f_2, \quad (2)$$

$$f_2 = d^2 f_{\text{tot}}, \quad (3)$$

where $f_{1,2}$ is the rate of detecting either one or two electrons per ICD event, f_{tot} is the real ICD event rate and d is the detection efficiency of each electron. The yields ($I_{1,2}$) of ICD electrons from observed one or two electron coincidences are then

$$I_1 = f_1 t, \quad (4)$$

$$I_2 = 2f_2 t, \quad (5)$$

where t is the measurement time, and the factor 2 comes from the fact that electron spectra for coincidences of two electrons contain the sum of both electrons. From the

ICD-related yield of coincidences including either a single electron or both electrons, we then determine the detection efficiency to be $\sim 20\%$. From the $>70\%$ open area ratio (OAR) of the MCPs, we would expect $\sim 30\%$ loss of electrons at the MCPs⁶⁰. Further loss of electrons happens at the mesh in front of the detector, and due to dependencies of the detection efficiency on the kinetic energy of the electrons⁶¹.

F. Detection of anions

Identification of ions by their time-of-flight in continuous experiments relies on coincidence detection. The simplest case is photoionization, as the electron flight time is negligible for mass spectrometry of the cations. Anion detection is of interest for example to study electron attachment processes.⁶² In He nanodroplets, electrons with relevant kinetic energies can be created by photoionization. After subsequent resonant⁶³ or dissociative⁶⁴ electron attachment, the formed anion will be detected in coincidence with the photoionized cation.

As a proof of concept for anion detection, we probed resonant $\text{O}_2 + h\nu \rightarrow \text{O}^+ + \text{O}^-$ pair formation at 17.47 eV photon energy^{65,66}. The cation flight time can be directly measured with photon energies above the appearance energy of O^+ . In case of pair formation, the event is triggered by O^- on the HEX75 detector and due to the longer flight time of the anion, the O^+ is observed at negative arrival time. The flight time of the coincident cation plus the negative arrival time axis thus gives the anion TOF spectrum and allows to set a cut on the O^- image that is shown in Fig. 16.

In such measurements of anion-cation coincidences, the primary photoelectrons should be suppressed. For this purpose we have added a simple construction to insert strong magnets near the ionization region. While leaving the anion TOF and image unperturbed, the electron count rate was re-

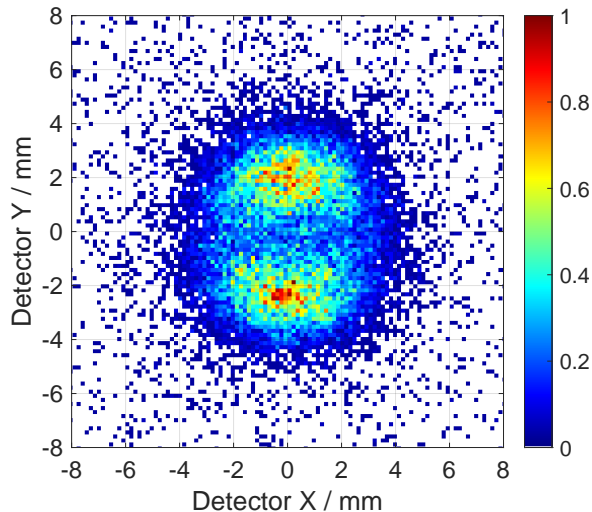


FIG. 16. Ion images of O^- ions detected in coincidence with O^+ following ion pair formation from O_2 at $h\nu = 17.47$ eV.

duced by half. We expect to improve the suppression of electrons by adding a second magnet tube on the opposite side.

IV. CONCLUSION AND OUTLOOK

In summary, we have described in detail a new endstation that complements the experimental capabilities of the AMOLine of the ASTRID2 synchrotron radiation facility. Using pure and doped He nanodroplets that were resonantly excited or ionized by XUV radiation, we characterized the performance of the imaging spectrometer with regard to high-resolution VMI photoelectron spectra, ion time-of-flight mass spectra, and spatial mapping of the ionization region. The capability of detecting electrons and ions in coincidence up to $e^-/e^-/ion/ion$ quadruple coincidences was demonstrated. Original multi-coincidence ICD electron spectra in the regimes of He-droplet double excitation and shake-up ionization were discussed. Furthermore, we presented measurements of oxygen anion/cation coincidences, electron angular distributions of pure He nanodroplets, and

fragment-ion mass spectra of thymine- D_2O complexes formed in He nanodroplets doped with thymine and water.

This endstation will be continuously upgraded in the following directions: A continuous cluster source for producing heavier rare-gas clusters and water clusters mixed with biomolecules is in preparation. The addition of an aerosol injector is planned. Simultaneous imaging of electrons and ions in a double imaging geometry^{11,12} is envisioned. The implementation of a IR-UV fluorescence spectrometer will further widen the scope of future experimental studies.

ACKNOWLEDGMENTS

The authors gratefully acknowledge financial support from Aarhus Universitets Forskningsfond (AUFF) and from the Carlsberg Foundation. The authors are particularly grateful for many insightful discussions with Robert Richter.

AUTHOR DECLARATIONS

The authors have no conflicts to disclose.

DATA AVAILABILITY STATEMENT

The data that support the findings of this study are available from the corresponding author upon reasonable request.

REFERENCES

- ¹P. Han, W. Martens, E. R. Waclawik, S. Sarina, and H. Zhu, *Particle & Particle Systems Characterization* **35**, 1700489 (2018).
- ²L. M. Liz-Marzán, C. J. Murphy, and J. Wang, *Chem. Soc. Rev.* **43**, 3820 (2014).
- ³C. Wang, S. K. Friedlander, and L. Mädler, *China Particuology* **3**, 243 (2005).

- ⁴K. T. Butterworth, S. J. McMahon, F. J. Currell, and K. M. Prise, *Nanoscale* **4**, 4830 (2012).
- ⁵A. T. J. B. Eppink and D. H. Parker, *Rev. Sci. Instrum.* **68**, 3477 (1997).
- ⁶G. A. Garcia, L. Nahon, C. J. Harding, E. A. Mikajlo, and I. Powis, *Rev. Sci. Instrum.* **76**, 053302 (2005).
- ⁷K. Hosaka, J. Adachi, A. V. Golovin, M. Takahashi, N. Watanabe, and A. Yagishita, *Jpn. J. Appl. Phys.* **45**, 1841 (2006).
- ⁸D. Rolles, Z. Pešić, M. Perri, R. Bilodeau, G. Ackerman, B. Rude, A. Kilcoyne, J. Bozek, and N. Berrah, *Nucl. Instrum. Meth. B* **261**, 170 (2007).
- ⁹X. Tang, X. Zhou, M. Niu, S. Liu, J. Sun, X. Shan, F. Liu, and L. Sheng, *Rev. Sci. Instrum.* **80**, 113101 (2009).
- ¹⁰P. O’Keeffe, P. Bolognesi, M. Coreno, A. Moise, R. Richter, G. Cautero, L. Stebel, R. Sergo, L. Pravica, Y. Ovcharenko, *et al.*, *Rev. Sci. Instrum.* **82**, 033109 (2011).
- ¹¹G. Garcia, B. Cunha de Miranda, M. Tia, S. Daly, and L. Nahon, *Rev. Sci. Instrum.* **84**, 053112 (2013).
- ¹²A. Bodi, P. Hemberger, T. Gerber, and B. Sztáray, *Rev. Sci. Instrum.* **83**, 083105 (2012).
- ¹³X. Tang, G. A. Garcia, J.-F. Gil, and L. Nahon, *Rev. Sci. Instrum.* **86**, 123108 (2015).
- ¹⁴O. Kostko, B. Xu, M. Jacobs, and M. Ahmed, *J. Chem. Phys.* **147**, 013931 (2017).
- ¹⁵K. Prince, P. Bolognesi, V. Feyer, O. Plekan, and L. Avaldi, *J. Electron Spectrosc. Relat. Phenom.* **204**, 335 (2015).
- ¹⁶K. Khistyayev, A. Golan, K. B. Bravaya, N. Orms, A. I. Krylov, and M. Ahmed, *J. Phys. Chem. A* **117**, 6789 (2013).
- ¹⁷B. Sztáray, K. Voronova, K. G. Torma, K. J. Covert, A. Bodi, P. Hemberger, T. Gerber, and D. L. Osborn, *J. Chem. Phys.* **147**, 013944 (2017).
- ¹⁸S. Schippers, A. D. Kilcoyne, R. A. Phaneuf, and A. Müller, *Contemporary Physics* **57**, 215 (2016).
- ¹⁹M. Simon, M. Schwarz, S. Epp, C. Beilmann, B. Schmitt, Z. Harman, T. Baumann, P. Mokler, S. Bernitt, R. Ginzler, *et al.*, *J. Phys. B: At., Mol. Opt. Phys.* **43**, 065003 (2010).
- ²⁰M. Niemeyer, K. Hirsch, V. Zamudio-Bayer, A. Langenberg, M. Vogel, M. Kosick, C. Ebrecht, K. Egashira, A. Terasaki, T. Möller, *et al.*, *Phys. Rev. Lett.* **108**, 057201 (2012).
- ²¹A. Kilcoyne, A. Aguilar, A. Möller, S. Schippers, C. Cisneros, G. Alna’Washi, N. Aryal, and K. Baral, *Phys. Rev. Lett.* **105**, 213001 (2010).
- ²²J. Shu, K. R. Wilson, M. Ahmed, and S. R. Leone, *Rev. Sci. Instrum.* **77**, 043106 (2006).
- ²³F. Gaie-Levrel, G. A. Garcia, M. Schwell, and L. Nahon, *Phys. Chem. Chem. Phys.* **13**, 7024 (2011).
- ²⁴M. Goldmann, J. Miguel-Sánchez, A. H. West, B. L. Yoder, and R. Signorell, *J. Chem. Phys.* **142**, 224304 (2015).
- ²⁵J. P. Toennies and A. F. Vilesov, *Angew. Chem. Int. Ed.* **43**, 2622 (2004).
- ²⁶M. Mudrich and F. Stienkemeier, *Int. Rev. Phys. Chem.* **33**, 301 (2014).
- ²⁷R. Fröchtenicht, U. Henne, J. Toennies, A. Ding, M. Fieber-Erdmann, and T. Drewello, *J. Chem. Phys.* **104**, 2548 (1996).
- ²⁸K. von Haeften, A. De Castro, M. Joppien, L. Moussavizadeh, R. Von Pietrowski, and T. Möller, *Phys. Rev. Lett.* **78**, 4371 (1997).
- ²⁹M. P. Ziemkiewicz, D. M. Neumark, and O. Gessner, *Int. Rev. Phys. Chem.* **34**, 239 (2015).
- ³⁰D. S. Peterka, A. Lindinger, L. Poisson, M. Ahmed, and D. M. Neumark, *Phys. Rev. Lett.* **91**, 043401 (2003).
- ³¹C. C. Wang, O. Kornilov, O. Gessner, J. H. Kim, D. S. Peterka, and D. M. Neumark, *J. Phys. Chem. A* **112**, 9356 (2008).
- ³²D. S. Peterka, J. H. Kim, C. C. Wang, and D. M. Neumark, *J. Phys. Chem. B* **110**, 19945 (2006).

- ³³D. Buchta, S. R. Krishnan, N. B. Brauer, M. Drabbels, P. O’Keeffe, M. Devetta, M. Di Fraia, C. Callegari, R. Richter, M. Coreno, *et al.*, *J. Phys. Chem. A* **117**, 4394 (2013).
- ³⁴L. Ben Ltaief, M. Shcherbinin, S. Mandal, S. Krishnan, A. LaForge, R. Richter, S. Turchini, N. Zema, T. Pfeifer, E. Fasshauer, *et al.*, *J. Phys. Chem. Lett.* **10**, 6904 (2019).
- ³⁵A. LaForge, M. Shcherbinin, F. Stienkemeier, R. Richter, R. Moshhammer, T. Pfeifer, and M. Mudrich, *Nat. Phys.* **15**, 247 (2019).
- ³⁶L. B. Ltaief, M. Shcherbinin, S. Mandal, S. Krishnan, R. Richter, T. Pfeifer, M. Bauer, A. Ghosh, M. Mudrich, K. Gokhberg, *et al.*, *Phys. Chem. Chem. Phys.* **22**, 8557 (2020).
- ³⁷M. Mudrich, A. LaForge, A. Ciavardini, P. O’Keeffe, C. Callegari, M. Coreno, A. Demidovich, M. Devetta, M. Di Fraia, M. Drabbels, *et al.*, *Nat. Commun.* **11**, 1 (2020).
- ³⁸A. C. LaForge, R. Michiels, Y. Ovcharenko, A. Ngai, J. Escartín, N. Berrah, C. Callegari, A. Clark, M. Coreno, R. Cucini, *et al.*, *Phys. Rev. X* **11**, 021011 (2021).
- ³⁹J. D. Asmussen, R. Michiels, K. Dulitz, A. Ngai, U. Bangert, M. Barranco, M. Binz, L. Bruder, M. Danailov, M. Di Fraia, J. Eloranta, R. Feifel, L. Giannessi, M. Pi, O. Plekan, K. C. Prince, R. J. Squibb, D. Uhl, A. Wituschek, M. Zangrando, C. Callegari, F. Stienkemeier, and M. Mudrich, *Phys. Chem. Chem. Phys.* **23**, 15138 (2021).
- ⁴⁰J. D. Asmussen, R. Michiels, U. Bangert, N. Sisourat, M. Binz, L. Bruder, M. Danailov, M. Di Fraia, R. Feifel, L. Giannessi, *et al.*, arXiv preprint arXiv:2203.01905 (2022).
- ⁴¹N. Hertel and S. V. Hoffmann, *Synchrotron Radiation News* **24**, 19 (2011).
- ⁴²M. Shcherbinin, A. C. LaForge, V. Sharma, M. Devetta, R. Richter, R. Moshhammer, T. Pfeifer, and M. Mudrich, *Phys. Rev. A* **96**, 013407 (2017).
- ⁴³L. F. Gomez, E. Loginov, R. Sliter, and A. F. Vilesov, *J. Chem. Phys.* **135**, 154201 (2011).
- ⁴⁴M. Förstel, M. Neustetter, S. Denifl, F. Lelievre, and U. Hergenbahn, *Rev. Sci. Instrum.* **86**, 073103 (2015).
- ⁴⁵O. Jagutzki, A. Cerezo, A. Czasch, R. Dörner, M. Hattas, M. Huang, V. Mergel, U. Spillmann, K. Ullmann-Pfleger, T. Weber, *et al.*, *IEEE Trans. Nucl. Sci.* **49**, 2477 (2002).
- ⁴⁶F. Österdahl, S. Rosén, V. Bednarska, A. Petignani, F. Hellberg, M. Larsson, and W. J. van der Zande, *J. Phys. Conf. Ser.* **4**, 286 (2005).
- ⁴⁷H. Hasegawa, A. Hishikawa, and K. Yamanouchi, *Chem. Phys. Lett.* **349**, 57 (2001).
- ⁴⁸“SIMION ion optics simulation software version 8.0, Idaho national engineering laboratory,” (2008).
- ⁴⁹M. Stei, J. von Vangerow, R. Otto, A. H. Kelkar, E. Carrascosa, T. Best, and R. Wester, *J. Chem. Phys.* **138**, 214201 (2013).
- ⁵⁰A. Wituschek, J. von Vangerow, J. Grzesiak, F. Stienkemeier, and M. Mudrich, *Rev. Sci. Instrum.* **87**, 083105 (2016).
- ⁵¹H. L. Offerhaus, C. Nicole, F. Lépine, C. Bordas, F. Rosca-Pruna, and M. J. J. Vrakking, *Rev. Sci. Instrum.* **72**, 3245 (2001).
- ⁵²D. Ferro, L. Bencivenni, R. Teghil, and R. Mastromarino, *Thermochim. Acta* **42**, 75 (1980).
- ⁵³A. C. LaForge, D. Regina, G. Jabbari, K. Gokhberg, N. V. Kryzhevoi, S. R. Krishnan, M. Hess, P. O’Keeffe, A. Ciavardini, K. C. Prince, R. Richter, F. Stienkemeier, L. S. Cederbaum, T. Pfeifer, R. Moshhammer, and M. Mudrich, *Phys. Rev. A* **93**, 050502 (2016).
- ⁵⁴G. Jabbari, K. Gokhberg, and L. S. Cederbaum, *Chem. Phys. Lett.* **754**, 137571 (2020).

- ⁵⁵M. Shcherbinin, F. V. Westergaard, M. Hanif, S. R. Krishnan, A. C. LaForge, R. Richter, T. Pfeifer, and M. Mudrich, *J. Chem. Phys.* **150**, 044304 (2019).
- ⁵⁶B. Dick, *Phys. Chem. Chem. Phys.* **16**, 570 (2014).
- ⁵⁷H. Kossmann, B. Krassig, and V. Schmidt, *J. Phys. B: At., Mol. Opt. Phys.* **21**, 1489 (1988).
- ⁵⁸M. Domke, K. Schulz, G. Remmers, G. Kaindl, and D. Wintgen, *Phys. Rev. A* **53**, 1424 (1996).
- ⁵⁹N. Sisourat, N. V. Kryzhevoi, P. Kolorenč, S. Scheit, T. Jahnke, and L. S. Cederbaum, *Nat. Phys.* **6**, 508 (2010).
- ⁶⁰K. Fehre, D. Trojanowskaja, J. Gatzke, M. Kunitski, F. Trinter, S. Zeller, L. P. H. Schmidt, J. Stohner, R. Berger, A. Czasch, *et al.*, *Rev. Sci. Instrum.* **89**, 045112 (2018).
- ⁶¹A. Müller, N. Djurić, G. Dunn, and D. Belić, *Rev. Sci. Instrum.* **57**, 349 (1986).
- ⁶²I. I. Fabrikant, S. Eden, N. J. Mason, and J. Fedor, *Adv. At. Mol. Opt. Phys.* **66**, 545 (2017).
- ⁶³S. Jaksch, I. Mähr, S. Denifl, A. Bacher, O. Echt, T. Märk, and P. Scheier, *Eur. Phys. J. D* **52**, 91 (2009).
- ⁶⁴F. F. da Silva, S. Jaksch, G. Martins, H. Dang, M. Dampc, S. Denifl, T. Märk, P. Limao-Vieira, J. Liu, S. Yang, *et al.*, *Phys. Chem. Chem. Phys.* **11**, 11631 (2009).
- ⁶⁵P. Dehmer and W. Chupka, *J. Chem. Phys.* **62**, 4525 (1975).
- ⁶⁶C. Zhou and Y. Mo, *J. Chem. Phys.* **139**, 084314 (2013).

A new endstation for extreme-ultraviolet spectroscopy of free clusters and nanodroplets

Supporting Information

Björn Bastian,¹ Jakob D. Asmussen,¹ Ltaief Ben Ltaief,¹ Achim Czasch,² Nykola Jones,¹ Søren V. Hoffmann,¹ Henrik B. Pedersen,¹ and Marcel Mudrich¹

¹*Department of Physics and Astronomy, Aarhus University, Ny Munkegade 120, 8000 Aarhus C, Denmark*

²*Institut für Kernphysik, Goethe Universität, Max-von-Laue-Strasse 1, 60438 Frankfurt, Germany*

(Dated: 11 April 2022)

S1. REFOCUSING OPTICS FOR THE ENDSTATION

The new endstation for extreme-ultraviolet spectroscopy of free clusters and nanodroplets is placed at the end of the existing ASTRID2 synchrotron radiation beam line, the AMOLine. To refocus the photon beam from the beam line into the sample region of the endstation, a toroidal mirror, MC2, is placed between the AMOLine and the endstation. The MC2 mirror images an intermediate focus (IF) in the AMOLine such that the distance from the IF to MC2 is 1080 mm and the distance from MC2 to the geometrical focus is 500 mm under a reflection angle of 88 degrees from the mirror surface normal. The mirror parameters are shown in Tables S.1 and S.2. Since the mirror is operated under a very grazing angle with the incoming beam 2 degrees from the mirror surface, and as the focus distance from the mirror is relatively short compared to the length of the mirror, the distance from the mirror where the beam size is smallest is shorter than the geometrical focus distance. To investigate the beam size as a function of the distance from the refocusing mirror, ray-tracing was done with Shadow¹ using a simulated undulator source and including all the optical elements in the AMOLine. The results are shown in Fig. S.1, and the minimum beam size is close to 400 mm from the mirror. When using the first harmonic of the undulator, the photon source is a single beam having a close to Gaussian shape, whereas the third harmonic of the undulator would have an angular distribution with a central cone and a ring of light at larger angles. To ensure that the use of the mirror at a distance of 400 mm from MC2, i.e. away from the geometrical focus, does not induce a multi-spot image of a third harmonic undulator source, both the first (10 eV) and the third harmonics of the undulator were ray-traced. They showed very similar sized and single-spot images. Therefore, based on these simulations, a distance of less than 500 mm from the MC2 mirror to the droplet beam can be used for the placement of the endstation resulting in smaller beam size. Due to space constraints in the experimental setup a final distance of 450 mm was chosen.

TABLE S.1. Geometry for the use of the mirror.

Object to mirror distance (r)	1080 mm
Mirror to Image distance (r')	500 mm
Reflection angle to mirror normal (α)	88°

TABLE S.2. Substrate shape parameters.

Shape type	Toroidal
Tangential radius (R)	19 600 mm (along long side of the mirror)
Sagittal radius (ρ)	23.85 mm (along short side of the mirror)
Optical active area	55 mm \times 10 mm

For comparison with spatial map imaging results we estimate the horizontal beam size at the position of the He droplet beam for 25 eV photon energy. The ray-tracing at 10 eV

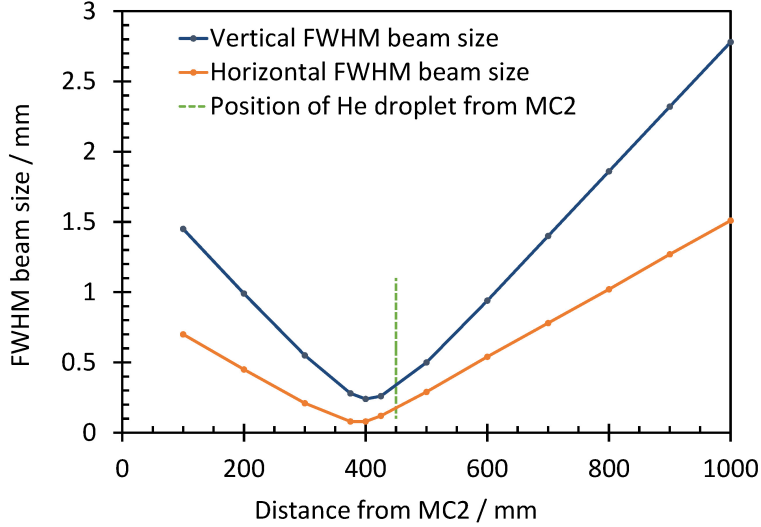


FIG. S.1. Beam size of the refocused photon beam as a function of the distance from the mirror.

photon energy yields ca. 0.18 mm FWHM in Fig. S.1. The diffraction limited beam size $\sigma_r \propto \sqrt{\lambda/L}$ with wavelength λ and undulator length L decreases with energy, and we thus expect a FWHM of 0.11 mm at 25 eV photon energy.

S2. NUMERICAL OPTIMIZATION FOR VELOCITY MAP IMAGING

To determine extractor electrode potentials for precise VMI without using the Einzel lens, the repeller R1 and R2 potentials in Fig. 3 (main article) are set to -3500 V. The maximum potential from the power supplies is -6 kV, so the chosen repeller potentials allow for cation acceleration in the TOF section up to 2500 eV kinetic energy which is more than sufficient for single ion detection with a MCP. The potentials of the three extractor electrodes E1–E3 are then adjusted to obtain optimal resolution. The Einzel lens potentials E4–E6 are kept at ground potential and the MCP front potential is 240 V for electron imaging. Using the SIMION-based VMI optimization routine published by Stei *et al.*² for an ion at rest in the center of the spectrometer yields the potentials E1 = -2867 V, E2 = -981 V and E3 = -391 V. The routine is based on computing the first and second order derivatives of impact position and time on the detector with respect to the initial position and velocity vectors. To optimize for two-dimensional VMI, the electrode potentials are then varied to optimize the target function

$$\left| \frac{\partial R}{\partial r} \right| + \left| \frac{\partial R}{\partial z} \right| + \left(\left| \frac{\partial R}{\partial v_r} \right| \right)^{-1} + \left| \frac{\partial R}{\partial v_z} \right| + \sum_{i,j=1}^4 \left| \frac{\partial^2 R}{\partial x_i \partial x_j} \right| \quad (1)$$

TABLE S.3. Alternative VMI potentials in V. Settings with lens use the Einzel lens electrodes with $E4 = E6$ and $E5 = 0V$. Otherwise $E5 = E6 = 0V$. (1), (2) and (3) denote numerical optimization for 0.5 eV, 30 eV and 70 eV kinetic energy ions. The linear calibration coefficient p_0 and the ratio between its simulated and experimental value are given in the last two columns.

Settings	R1	E1	E2	E3	E4	Exp. p_0	Sim./Exp.
3.5 kV lens (3)	-3500	-2628	-1359	71	3500	0.0331(3)	1.09
6.0 kV lens (3)	-3500	-2634	-1152	-388	6000	0.0505(3)	1.37
Non-opt. lens	-3500	-2867	-981	-391	6000	0.0602(3)	1.06
No lens 50 %	-1750	-1433.5	-490.5	-195.5	0	0.012 22(7)	0.96
No lens	-3500	-2867	-981	-391	0	0.023 48(14)	1.004
with E4 (1)	-3500	-3240	-2935	-2397	-1308		
with E4 (2)	-3500	-3236	-2929	-2419	-1380	0.0237(2)	1.03

with $\{x_i\} = \{r, z, v_r, v_z\}$ where R denotes the detector radius at the impact position and the x_i the initial position r , z and velocities v_r , v_z in cylinder coordinates. The z -axis is parallel to the symmetry axis of the spectrometer. The target function could be refined by explicitly taking into account the initial spatial broadening and velocity spread of the ions, which however has its limits by the enforced rotational symmetry about the detector axis and the dependence of the velocity distribution on the probed process. Instead, we follow the generic procedure by Stei *et al.*: The choice of native units with all quantities on the order of magnitude 1 allows to set all prefactors to 1. Therefore, Eq. (1) mixes different units and dimensions but is able to roughly homogeneously suppress the different factors that otherwise contribute to broadening of the desired velocity mapped distribution.

The simplest approach to increase the kinetic energy acceptance is the scaling of a set of VMI potentials to reduce the impact radii on the detector. The maximum available potential with the current power supplies is 6 kV. Increasing the repeller potential is thus limited to about 4 kV by the requirement of about 2 kV acceleration for ion detection in case of coincidence measurements. Instead, up to 90 eV kinetic energy acceptance is achieved by using the Einzel lens electrodes with the central electrode on ground (close to the MCP front potential) and the outer electrodes on high positive potentials to temporarily accelerate the electrons and thus compress the spatial distribution on the detector. To determine VMI potentials with the Einzel lens, the previously optimized potentials were modified by adding a fixed potential to the Einzel lens electrodes E4 and E6 (see Fig. 3 in the main article) and then reoptimized for the extractor potentials E1, E2 and E3 to restore good VMI conditions, that is, a small dependence from the initial position of the imaged particle. In contrast to the originally published optimization routine, the first and second order derivatives were typically evaluated at non-zero initial kinetic energies as specified for the different optimization results in Table S.3.

Simulations have shown that evaluating the derivatives for the numerical optimization at different initial kinetic energies yields VMI potentials that have the optimal spatial focusing at different detector radii. This has not found to be significant in the empiric characterizations, which has been explained by the spatial resolution of the detector system that determines the energy resolution at low detector radii. Optimizations at non-zero kinetic energy are still useful to obtain potentials that are theoretically less sensitive to the initial position and with calibration functions that deviate less from linearity.

All optimization results were obtained for an initial design that included a mesh at the exit side of electrode E6. Without the mesh, the magnification is reduced and the initial kinetic energy of 70 eV (see caption to Table S.3) corresponds to a new value of 59 eV with the same impact radius on the detector. Potentials without the Einzel lens do not depend on the presence of the mesh. Reoptimizations without the mesh for VMI settings with the Einzel lens give similar results and are expected to also be comparable to the presented results with respect to energy resolution.

For the standard potentials without compression, the first electrode E4 of the Einzel lens section can be used to further improve the VMI focusing conditions. Two such settings are listed in Table S.3. The weaker extraction potential however reduces the time of flight resolution. It has not been tested if optimization at nonzero kinetic energies could further improve the resolution of the 100% potentials without E4 and keeping the steeper extraction potential. The potentials with E4 from optimization at 0.5 eV kinetic energy were systematically varied to check, if the optimization results match optimal empirical results in terms of energy resolution. Only the E1 potential turned out to be important and matched the optimum up to 20 V precision. Variations of the E1 potential could not improve the overall energy resolution in calibration measurements in a significant way.

The measured and simulated linear calibration factors p_0 are given in the last columns of Table S.3. Discrepancies are on the order of 5% or smaller, but increase in case of the optimized settings with high Einzel lens potentials up to 9 and 37%.

S3. ENERGY CALIBRATION FOR VELOCITY MAP IMAGING

VMI maps an electron moving perpendicular to the spectrometer axis (slice distribution) with a specific kinetic energy E_{kin} onto a specific radius R on the detector. A three-dimensional momentum vector distribution with cylindrical symmetry results in an Abel transformed image on the detector such that the slice distribution can be reconstructed by Abel inversion. Assuming an analytical dependence of the kinetic energy on the radius and symmetry about the spectrometer axis, only even powers in a Taylor expansion are allowed,

which in 3^{rd} order gives

$$E_{\text{ph}} = E_0 + p_0 (R^2) + p_1 (R^2)^2 + p_2 (R^2)^3 \quad (2)$$

for the photon energy, where E_0 is the ionization potential of helium. For each photon energy, the radius of impact on the detector R is obtained from a Gaussian fit to the radial distribution of the Abel inverted image. The inversion is performed with the Maximum Entropy Velocity Legendre Reconstruction (MEVELER) method³. Fitting Eq. (2) to the results in Fig. 5a yields the coefficients in Table II with residuals $< 1\%$. Simulation results were obtained for centered ions with velocity vectors perpendicular to the spectrometer axis without an inversion step.

The calibration data are also useful to determine the resolution $\Delta E/E$ as a function of kinetic energy. All calibration and energy resolution related data were measured in a row. This allows reliable comparisons of different VMI potentials with otherwise identical conditions. The energy resolution could not always be reproduced between different beamtimes.

S4. ENERGY RESOLUTION WITH VELOCITY MAP IMAGING

To assess the VMI energy resolution from simulations, detector images have been computed for groups of 15 000 particles with the same kinetic energy. The initial velocity direction and positions were uniformly sampled from a 4π solid angle and a cylinder with 4 mm length, corresponding to the width of the He droplet beam (along the photon beam), and a radius of 0.2 mm of the refocused photon beam, corresponding to 4 standard deviations of its radial profile. The spatial distribution of the impact positions was binned in $0.1 \text{ mm} \times 0.1 \text{ mm}$ squares and Abel inverted. The energy resolution was obtained from the standard deviation and position of a Gaussian fit to the resulting radial distribution according to Gaussian error propagation as $\Delta E/E = 2 \Delta r/r$ with the radius r on the detector.

S5. SPATIAL MAP IMAGING

The spectrometer can be operated at different potentials to image positions in the interaction region with high precision² instead of performing velocity map imaging. Table S.4 summarizes electrode potentials before and after optimization for spatial map imaging (SMI) along with the relation between the radial impact position on the detector R and the initial position r and radial velocity v_r of the ion. While the magnification factor $\partial R/\partial r$ stays similar, the effect of the initial velocity, in first order $\partial R/\partial v_r$, is substantially reduced. This effect could be confirmed by the observation of sharper SMI images.

TABLE S.4. Empirical and simulated SMI potentials in V and first derivatives of the impact position R with respect to initial r , v_r . Space and velocity units are mm and $\text{mm } \mu\text{s}^{-1}$.

Settings	R1	E1	E2	E3	$\partial R/\partial r$	$\partial R/\partial v_r$
Empirical	3500	3495	3230	0	-3.395	0.256
Optimized	3500	3469	3456	213	-3.154	-0.001

TABLE S.5. Alternative SMI potentials in V. Magnifying potentials map radial positions r with $\partial R/\partial r = -13.34$ and TOF-SMI maps axial positions z with $\partial T/\partial z = 58.3 \text{ ns mm}^{-1}$.

Settings	R1	E1	E2	E3	E4	E5
Magnified	3500	-2939	2726	-1106	0	262
TOF-SMI	3500	1073	-3498	334	680	0

With different initial potentials or target functions in the optimization, alternative settings were obtained to achieve larger magnification or to perform one-dimensional SMI using the ion time of flight. The potentials are given in Table S.5. The simulated magnification of -13.34 is about four times larger than before but at the cost of a significant derivative $\partial R/\partial v_r = 3.28 \mu\text{s}$. The scaling factor for the TOF-SMI is 58.3 ns mm^{-1} and the first order influence of the ion velocity on the arrival time is $\partial T/\partial v_z = -1.8 \text{ ns } \mu\text{s mm}^{-1}$.

Simulated and measured magnification factors for electron and cation SMI as well as widths of the spatial distributions are given in Table S.6. They are discussed with regard to the achieved SMI resolution in the main article.

TABLE S.6. SMI magnification factors from K-doped HND ionized at 767 nm. Empirical and simulated values as well as the relative deviation and widths of the spatial distributions orthogonal to the ionization laser are given for different SMI potentials and for cation and electron imaging.

SMI setting	Species	Empiric factor	Simulated factor	Deviation	Width/mm
SMI 1D	K^+	64.0 ns/mm	58.3 ns/mm	10 %	0.050
SMI 2D (magn.)	K^+	-13.0	-13.34	2.6 %	0.050
SMI 2D (100 %)	K^+	-3.200	-3.154	-1.5 %	0.050
SMI 2D (100 %)	e^-	-3.203	-3.154	-1.6 %	0.08
SMI 2D (50 %)	e^-	-3.202	-3.154	-1.5 %	0.11

The real positions in Fig. 8 from SMI of He^+ in the main article are determined with the calibration factor -3.2 and with respect to the zero point $x_0 = 0.43$, $y_0 = 0.5$. The zero point of the spectrometer was determined as the center of the photoelectron rings in an electron VMI calibration measurement of an atomic He beam. The systematic error of the zero point determination due to the center of mass velocity of the He beam should be small because of the low electron mass and consequently short flight time to the detector. Using the estimate of 560 m s^{-1} for the maximum speed of an ideal supersonic expansion of He at 30 K, a SIMION trajectory yields a deviation of $5 \mu\text{m}$.

S6. CORRECTION OF THE BACKGROUND SUBTRACTION FACTOR

For total electron distributions, the background is subtracted from the foreground with a weight of 1, if the acquisition durations are identical. Conditions to the data that restrict the hit statistics, for instance to analyze only single hits, are typically more restrictive to the foreground than to the lower count rate background data and require the correction

$$I_{\text{subtracted}} = I_{\text{fg}} - \frac{T_{\text{fg}}}{T_{\text{bg}}} \frac{N_{\text{bg,all}}}{N_{\text{fg,all}}} \frac{N_{\text{fg,restr}}}{N_{\text{bg,restr}}} I_{\text{bg}} \quad (3)$$

with time intervals T_x of the chopper wheel period that are collected into foreground ($x = \text{fg}$) and background ($x = \text{bg}$) data, the total electron counts $N_{x,\text{all}}$ and the restricted electron counts $N_{x,\text{restr}}$.

REFERENCES

- ¹B. Lai and F. Cerrina, Nucl. Instrum. Meth. A **246**, 337 (1986).
- ²M. Stei, J. von Vangerow, R. Otto, A. H. Kelkar, E. Carrascosa, T. Best, and R. Wester, J. Chem. Phys. **138**, 214201 (2013).
- ³B. Dick, Phys. Chem. Chem. Phys. **16**, 570 (2014).